# REVIEW ARTICLE

# Topological nodal line semimetals predicted from first-principles calculations

**Rui Yu[1,*], Zhong Fang[2,3], Xi Dai[2,3], Hongming Weng[2,3,†]**

[1]*School of Physics and Technology, Wuhan University, Wuhan 430072, China*
[2]*Beijing National Laboratory for Condensed Matter Physics, and Institute of Physics,*
*Chinese Academy of Sciences, Beijing 100190, China*
[3]*Collaborative Innovation Center of Quantum Matter, Beijing 100190, China*
*Corresponding authors. E-mail: *yurui1983@foxmail.com, †hmweng@iphy.ac.cn*

Topological semimetals are newly discovered states of quantum matter, which have extended the concept of topological states from insulators to metals and attracted great research interest in recent years. In general, there are three kinds of topological semimetals, namely Dirac semimetals, Weyl semimetals, and nodal line semimetals. Nodal line semimetals can be considered as precursor states for other topological states. For example, starting from such nodal line states, the nodal line structure might evolve into Weyl points, convert into Dirac points, or become a topological insulator by introducing the spin–orbit coupling (SOC) or mass term. In this review paper, we introduce theoretical materials that show the nodal line semimetal state, including the all-carbon Mackay–Terrones crystal (MTC), anti-perovskite $Cu_3PdN$, pressed black phosphorus, and the $CaP_3$ family of materials, and we present the design principles for obtaining such novel states of matter.

**Frontiers of Physics**

## Contents

## 1 Introduction

The study of topological states has become one of the most critical physical phenomena in condensed matter physics. It began with the discovery of two-dimensional (2D) and three-dimensional (3D) topological insulators approximately a decade ago, and it has recently been extended to metal states, or more precisely, semimetal states. In the ideal case, the Fermi surface in topological semimetals contains isolated band-crossing points or lines, rather than surface in normal metals. Such band-crossing points result from band inversion and behave as the monopoles of Berry flux [1, 2], causing quantized Berry flux on the enclosed Fermi surface that surrounds the nodal point [1, 3] or $\pi$ Berry phase along a loop that threads the nodal line [1, 4, 5]. These quantized numbers can be taken as the topological invariant to identify the band topology of corresponding metals.

Thus far, three types of nontrivial topological semimetals have been proposed. Based on the degeneracy of the band-crossing points and their distribution in the Brillouin zone (BZ), the types of semimetals are Weyl semimetals [6–9], Dirac semimetals [10, 11], and nodal line semimetals [1, 12, 13], all of which have band-crossing points due to band inversion [14]. The Dirac semimetal, which can be regarded as a three-dimensional version of graphene, has been theoretically proposed and experimentally confirmed in $Na_3Bi$ and $Cd_3As_2$ [10, 11, 15–19]. In these two materials, the bands cross near the Fermi energy and form Dirac points with

---

fourfold degeneracy. The band-crossing points are protected by crystalline symmetry. Gibson *et al.* has discussed the general design principles of 3D Dirac semimetals from symmetry consideration and predicted a series of Dirac semimetals [20]. For Weyl semimetals, the band-crossing points are double degenerate with definite chirality and are located at an even number of discrete points in the BZ, which have been theoretically predicted [21–23] and experimentally verified in the TaAs family of materials [24–29]. There has been much progress in the discovery of Weyl semimetals recently, such as the proposed non-magnetic Weyl semimetal in chalcopyrites including the $Ta_3S_2$ [30] and $CuTlSe_2$ family of materials [31], HgTe-class materials [32], magnetic Weyl semimetals in half-Heuslers under a magnetic field [33] and magnetic Heuslers [34], type-II Weyl semimetal in $MoP_2$, and $WP_2$ [35].

In topological nodal line semimetals [36], the band-crossing points form closed loops instead of discrete points in the momentum space. Recently, many materials showing these topological states have been theoretically proposed, including Bernal graphite [37–39], the all-carbon Mackay–Terrones crystal (MTC) [40], hyper-honeycomb lattices [41], 3D-honeycomb lattices [42], $Ca_3P_2$ [43, 44], LaN [45], $Cu_3$(Pd,Zn)N [46, 47], the inter-penetrated graphene network [48], (Tl,Pb)TaSe$_2$ [49, 50], ZrSiS [51], perovskite iridates [52–55], CaAgX (X=P,As) [56], BaMX$_3$ (M=V, Nb, Ta; X=S, Se) [57], black phosphorus under pressure [58], CaP$_3$ [59], fcc calcium, fcc strontium, fcc ytterbium [60], body-centered orthorhombic C$_{16}$ [61], hcp alkali earth metals (Be, Mg, Ca, and Sr) [62], and some 2D materials [63, 64].

Some novel properties have been proposed for nodal line semimetals, including the nearly flat drumhead-like surface states [40, 46, 47, 65], which have opened an important route for achieving high-temperature superconductivity [66–68], the unique Landau energy level [69], and special collective modes from the novel nodal line structure [70]. The nodal line structure can also be considered as precursor states for many topological states. For example, starting from a nodal line semimetal, the inclusion of spin–orbit coupling (SOC) will lead to the evolution of the nodal ring into Weyl nodes (such as in the TaAs family of materials), drive the nodal rings into Dirac nodes (such as in anti-perovskite $Cu_3PdN$), or open a gap to convert the nodal line semimetal into a topological insulator (such as in MTC and $Ca_3P$). In this review, we will summarize our theoretical proposals for nodal line semimetal materials.

# 2 Nodal line semimetal materials

In this section, we briefly summarize our theoretical material proposals for nodal line semimetals, including the

all-carbon MTC, anti-perovskite $Cu_3PdN$, black phosphorus, and the $CaP_3$ family of materials. By introducing these four materials, we present the design principles of nodal line states for spin-less systems. The low-energy k·p models, constructed from the symmetry consideration of each system, are used to understand the nodal line structure and surface states.

## 2.1 All-carbon Mackay–Terrones crystal

Mackay and Terrones have investigated models of periodic minimal surface building from graphite-like sheets [71]. The simplest surface is shown in Fig. 1(a), which is called the P-surface of Schwarz. This structure, labeled as 6-1-1-p MTC, has 176 atoms per unit cell with space group $Pm\bar{3}m$ (No. 221). In this section, we briefly introduce the electronic structure of MTC and discuss the nodal line states in this system.

We first consider the band structure without SOC. First-principles calculations show that the low-energy occupied and unoccupied bands are triply degenerate and have $T_{1g}$ and $T_{2u}$ symmetry at the $\Gamma$ point, respectively, as shown in Fig. 1(d). The parity of the $T_{1g}$ bands are even, while it is odd for $T_{2u}$ bands. At the $R$ point, the low-energy bands, which are still grouped as $T_{1g}$ and $T_{2u}$,
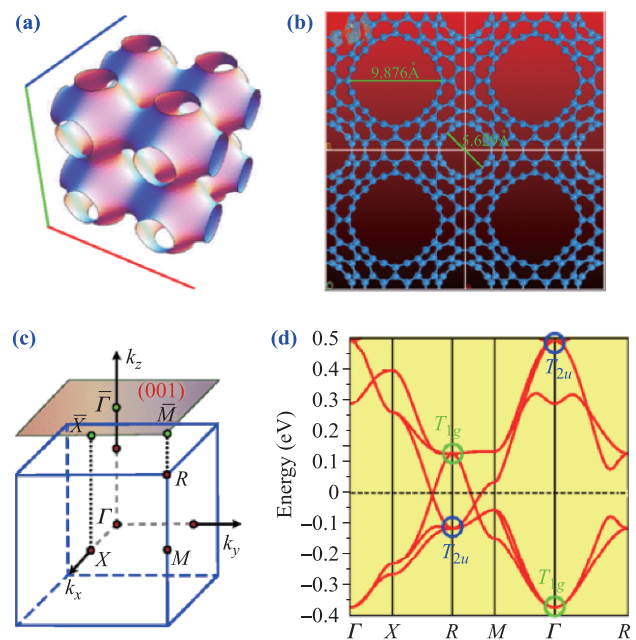


**Fig. 1** (a) The Schwarz minimal P surface in a $2 \times 2 \times 2$ supercell. (b) The top view of a 6-1-1-p MTC in a $2 \times 2$ supercell. (c) Bulk and (001)-surface BZ, as well as the highly symmetrical points. (d) Band structure from the first-principles calculation. The two triply degenerate eigenstates at $\Gamma$ and $R$ with $T_{1g}$ and $T_{2u}$ symmetrical representation are marked. The band inversion between them can be easily seen. Reproduced from Ref. [40].

exchange their energy order. This type of inverted band structure is the key characteristic of topological insulators. The inverted bands cross near the Fermi energy, as shown in Fig. 1(d). Usually, these crossing points are gaped because of the coupling between the two sets of bands. However, in MTC, the cross points are stable and form closed loops as shown in Fig. 3, which are protected by time-reversal symmetry and inversion symmetry as explained later. The SOC will open a band gap approximately 0.13 meV (or 1.5 K) along the nodal Line, and the system becomes a topological insulator with the $Z_2$ index (1;111). However, the SOC-induced gap can be neglected in cases with temperature greater than 1.5 K, and we ignore the SOC in MTC in the following discussions.

In order to simplify the discussion, we consider a single unit cell of MTC as an isolated carbon molecule with approximate spherical symmetry. The MTC can be viewed as a cubic lattice consisting of such carbon molecules. The orbitals of each carbon molecule are chosen with $T_{1g}$ and $T_{2u}$ symmetry, which can be viewed as atomic orbitals with g- and f-wave symmetry under the cubic crystal field. By checking the character table of the point group at the $\Gamma$ point, we can find that the $T_{1g}$ sector consists of $g_{xy(x^2-y^2)}$, $g_{yz(y^2-z^2)}$, and $g_{zx(z^2-x^2)}$ orbitals, which are a subgroup of $g$ orbitals split under a cubic crystal field. The $T_{2u}$ sector contains $f_{x(y^2-z^2)}$, $f_{y(z^2-x^2)}$, and $f_{z(x^2-y^2)}$ orbitals from $f$ orbitals. Thus, from the basis of these six hypothetical atomic orbitals, a Slater–Koster-type tight-binding (TB) Hamiltonian can be established. Some of the nonzero elements of the Hamiltonian are listed below.

$$
\begin{aligned}
H_{g_{xy(x^2-y^2)},g_{xy(x^2-y^2)}} &= +2V_{ggp}(\cos k \cdot a_x + \cos k \cdot a_y) \\
&\quad +2V_{ggd}\cos k \cdot a_z + E_g,
\end{aligned}
$$
$$
H_{g_{xy(x^2-y^2)},f_{x(y^2-z^2)}} = \mathrm{i}2(V_{fgp} + V_{fgd})\sin k \cdot a_y,
$$
$$
H_{g_{xy(x^2-y^2)},f_{y(z^2-x^2)}} = \mathrm{i}2(V_{fgp} + V_{fgd})\sin k \cdot a_x
$$
$$
\begin{aligned}
H_{f_{x(y^2-z^2)},f_{x(y^2-z^2)}} &= E_f + 2(V_{ffp} + V_{ffd})\cos k \cdot a_x \\
&\quad -2(V_{ffp} + V_{ffd})\cos k \cdot a_y \\
&\quad -2(V_{ffp} + V_{ffd})\cos k \cdot a_z, \quad (1)
\end{aligned}
$$

where $a_x$, $a_y$, and $a_z$ are the nearest-neighbor sites along the positive $x$, $y$, and $z$ directions, respectively. $V_{ggp}$ is the nearest-neighbor hopping parameter between $g_{xy(x^2-y^2)}$ orbitals in the $x$ and $y$ directions, while $V_{ggd}$ is the hopping parameter in the $z$ direction. $V_{ffp}$ is the hopping parameter between $f_{xy^2}$ $(-f_{xz^2})$ along $x$ and $y$ ($x$ and $z$), while $V_{ffd}$ is the hopping parameter along the $z$ direction. $V_{fgp}$ ($V_{fgd}$) is the hopping parameter between $g_{xy(x^2-y^2)}$ and $f_{xy^2}$ $(-f_{xz^2})$ along the $y$ direction. $E_f$ and $E_g$ are the on-site energies. The matrix elements not shown in the above equations can be derived using the cubic cyclic symmetry. With this TB model, we can well reproduce the lower energy bands of
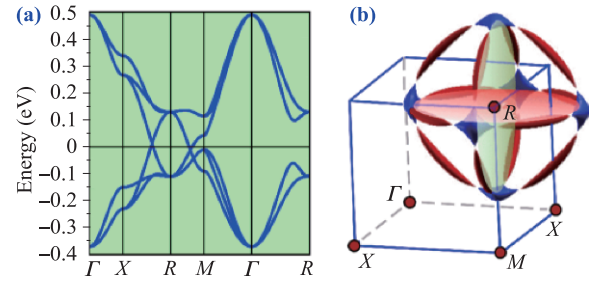
**Fig. 2** **(a)** Band structure calculated from effective TB Hamiltonian Eq. (1). The Slater–Koster parameters are obtained by fitting the band structure from the first-principles calculations and the values are listed as (in eV) $E_g = -0.12$, $E_f = 0.19$, $V_{ffp} = 0.019$, $V_{ffd} = -0.075$, $V_{fgp} = 0.05$, $V_{fgd} = 0.0$, $V_{ggp} = -0.035$, and $V_{ggd} = -0.055$. This model Hamiltonian reproduces all the features of Fig. 1(d). **(b)** The Fermi surface consists of three lotus-root-like rings. These rings are center the $R$ point and are parallel to the $k_x = \pi/a$, $k_y = \pi/a$, and $k_z = \pi/a$ plane, respectively. They are formed by the electron pockets (*blue*) and hole pockets (*red*) connected by nodal points at the Fermi energy. Reproduced from Ref. [40].
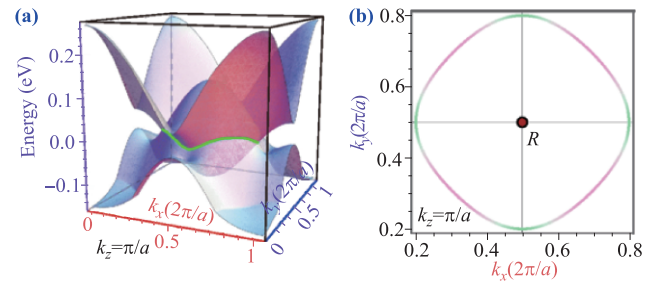


**Fig. 3** **(a)** Band crossings of the two bands near the Fermi level form nodal line (*in green*) in the $k_z = a$ plane. **(b)** The crossing happens at different eigen-energies as indicated by different colors, where greener denotes lower in energy. Reproduced from Ref. [40].

MTC, as shown in Fig. 2(a). The Fermi surface consists of three lotus-root-like rings. These rings surround the $R$ point and are parallel to the $k_x = \pi/a$, $k_y = \pi/a$, and $k_z = \pi/a$ planes, respectively. They are formed by the electron pockets (blue) and hole pockets (red) connected by nodal points at the Fermi energy, as shown in Fig. 2(b).

The band inversion and nodal line structure suggest that the novel surface states appear on the surface of materials. In order to calculate such surface states, we construct a thick slab along the (001)-direction using the TB model. The obtained surface states, which are nearly flat in energy, are shown in Fig. 4, and it is nestled between two solid Dirac cones, which are the projections of the nodal line circles in the (001)-direction. The bandwidth of the surface state is approximately 40 meV owing to the particle-hole asymmetry. The peak-like surface
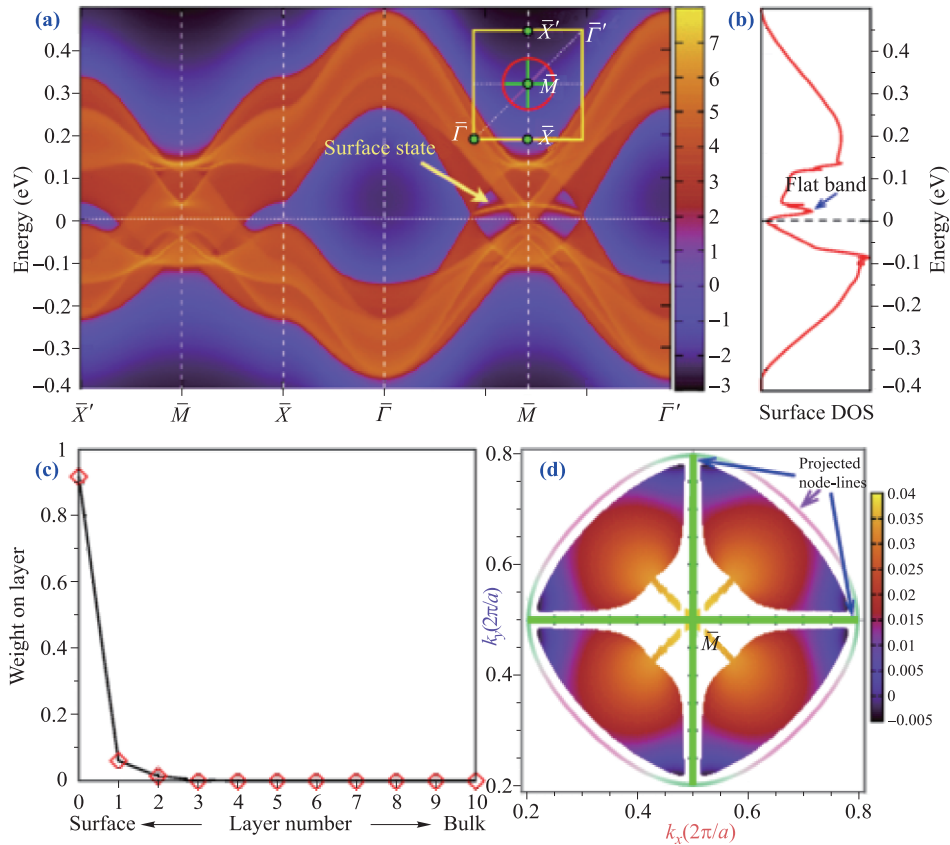
**Fig. 4** The (001)-surface state. **(a)** The nearly flat surface band is nestled between two solid Dirac cones, which are the projection of one of the nodal line circles as indicated in the inset (*red circle*). The other two nodal line rings are projected as two orthogonal diameters (*green line*). **(b)** The surface density of state. **(c)** The wave function of the surface state indicated by the arrow decays rapidly into bulk. **(d)** The eigen-energy distribution of a surface flat band nestled inside of a projected nodal line circle, which looks like a vibration model of a "drumhead". The mixing of surface and bulk states leads to discontinuity in this plot. Reproduced from Ref. [40].

density of states contributed by this nearly flat band is clearly shown in Fig. 4(b), which is proposed to be an important route to high-temperature surface superconductivity [66]. The layer-resolved weight of the wave function for the surface flat band is shown in Fig. 4(c). It penetrates only three layers into the bulk with most of the weight on the surface layer. The surface localization of these flat bands is well resolved for those separated from bulk bands. The surface states in the surface BZ are shown in Fig. 4(d), which appears like a drumhead. Such drumhead-like states are readily detected by angle-resolved photo-electron spectroscopy or scanning tunneling microscopy.

In order to understand the nodal line structure in MTC more clearly, we construct an effective $2 \times 2$ model Hamiltonian near the $R$ point, which can be generally expressed in the following form:

$$H(\boldsymbol{k}) = g_0(\boldsymbol{k}) + g_1(\boldsymbol{k})\sigma_x + g_2(\boldsymbol{k})\sigma_y + g_3(\boldsymbol{k})\sigma_z, \quad (2)$$

where the Pauli matrices $\sigma_i$ denote the space of the

two crossing bands, one with positive parity and the other with negative parity. The symmetry group at the $R$ point contains inversion symmetry and time-reversal symmetry, as well as crystalline cubic symmetry. The inversion symmetry constrains the Hamiltonian satisfying

$$\hat{P}H(\boldsymbol{k})\hat{P}^{-1} = H(-\boldsymbol{k}). \quad (3)$$

Consequently, $g_{0,3}(\boldsymbol{k})$ are even functions of $\boldsymbol{k}$ and $g_{1,2}(\boldsymbol{k})$ are odd functions of $\boldsymbol{k}$. On the other hand, the time-reversal symmetry requires that

$$\hat{T}H(\boldsymbol{k})\hat{T}^{-1} = H(-\boldsymbol{k}), \quad (4)$$

where $\hat{T} = K$ and $K$ is the complex-conjugate operator for the spin-less case. This requirement leads to $g_{0,1,3}(\boldsymbol{k})$ being even and $g_2(\boldsymbol{k})$ being odd. By combining the constraints with $g_i(\boldsymbol{k})$s, we obtain that $g_1(\boldsymbol{k}) = 0$, $g_{0,3}(\boldsymbol{k})$ are even functions of $\boldsymbol{k}$, and $g_2(\boldsymbol{k})$ is an odd function of $\boldsymbol{k}$. Considering the cubic symmetry at the $R$ point, we

have

$$g_0(\boldsymbol{k}) = a_0 + a_1(k_x^2 + k_y^2 + k_z^2),$$
$$g_2(\boldsymbol{k}) = \gamma k_x k_y k_z,$$
$$g_3(\boldsymbol{k}) = m_0 + b(k_x^2 + k_y^2 + k_z^2), \tag{5}$$

up to the lowest order of $\boldsymbol{k}$. The eigenvalues of Eq. (2) are $E(\boldsymbol{k}) = g_0(\boldsymbol{k}) \pm \sqrt{g_2^2(\boldsymbol{k}) + g_3^2(\boldsymbol{k})}$. The nodal lines appear when $g_2(\boldsymbol{k}) = 0$ and $g_3(\boldsymbol{k}) = 0$. It is easy to check that $g_3(\boldsymbol{k}) = 0$ can be satisfied only in the case of $m_0 b > 0$, which is nothing but the band-inversion condition. When band inversion occurs, there always exist closed nodal lines in momentum space, as shown in Fig. 3, which are the solutions of $g_2(\boldsymbol{k}) = g_3(\boldsymbol{k}) = 0$, and there are three nodal lines due to the cubic symmetry. The nodal lines are not necessarily flat in energy, and they can have energy dispersion in the k space, as shown in Fig. 3, which is determined by the $g_0(\boldsymbol{k})$ term.

The drumhead-like surface states can also be obtained using the $k \cdot p$ model in Eqs. (2) and (5), as discussed below. We consider a surface terminated in the $z$ direction. In this case, $k_z$ is perpendicular to the surface and $k_{x,y}$ are parallel to the surface. Following the method proposed in Ref. [72], the Dirac Hamiltonian in Eq. (2) can be expressed as

$$H(k_x, k_y, k_z) = g_0(\boldsymbol{k}) + \boldsymbol{h}(\boldsymbol{k}) \cdot \boldsymbol{\sigma}, \tag{6}$$

where

$$\boldsymbol{h}(\boldsymbol{k}) = \boldsymbol{c}^0(k_x, k_y) + \boldsymbol{c}^1(k_x, k_y)k_z + \boldsymbol{c}^2(k_x, k_y)k_z^2, \tag{7}$$

and

$$\boldsymbol{c}^0 = (0, 0, m_0 + b(k_x^2 + k_y^2)),$$
$$\boldsymbol{c}^1 = (0, \gamma k_x k_y, 0),$$
$$\boldsymbol{c}^2 = (0, 0, b). \tag{8}$$

The behavior of $\boldsymbol{h}(\boldsymbol{k})$ completely determines the topological nature of the system, and it is the key to understand the relation between the existence of surface states and bulk topological properties. By tuning $k_z$, the vector $\boldsymbol{h}(\boldsymbol{k})$ forms a parabola in the 2D plane spanned by $\boldsymbol{c}^1$ and $\boldsymbol{c}^2$. As proved in Ref. [72], for the continuum Hamiltonian $\boldsymbol{h}(\boldsymbol{k})$, the surface states exist if the origin is within the concave side of the parabola, leading to the following inequality:

$$\frac{m_0}{b} + (k_x^2 + k_y^2) < 0. \tag{9}$$

for $k_x$ and $k_y$. The above inequation indicates that the surface state exists inside the area of the projected nodal line. The energy of the surface states (located on the surface of a semi-infinite slab with $z \geq 0$) can then be calculated as

$$E_s = \boldsymbol{c}^0 \cdot \frac{\boldsymbol{c}^1 \times \boldsymbol{c}^2}{|\boldsymbol{c}^1 \times \boldsymbol{c}^2|}. \tag{10}$$

As expressed in Eq. (8), $\boldsymbol{c}^0$ is in the plane spanned by vectors $\boldsymbol{c}^1$ and $\boldsymbol{c}^2$; therefore, $\boldsymbol{c}^0$ is perpendicular to $\boldsymbol{c}^1 \times \boldsymbol{c}^2$, which leads to $E_s = 0$. This result indicates that a dispersion-less state can exist on the surface of a nodal line semimetal within the area determined by Eq. (9). The topological trivial term $g_0(\boldsymbol{k})$ in Eq. (6) will introduce a finite dispersion and finally lead to drumhead-like surface sates, as shown in Figs. 4(a) and (d).

## 2.2 Anti-perovskite Cu₃PdN

In this section, we briefly review the nodal line structure proposed for cubic anti-perovskite $Cu_3PdN$. The crystal structure of $Cu_3PdN$ is shown in Fig. 5(a), where nitrogen atom is at the center of the cube and is surrounded by octahedral Cu atoms and Pd is located at the corner of the cube. The symmetry of $Cu_3PdN$ is $Pm\bar{3}m$ (No. 221), which is the same as that of MTC.

First-principles calculations show that the low-energy states of $Cu_3PdN$ are dominated by Pd $4d$ (blue) and Pd $5p$ (red) orbitals and the band inversion occurs at the $R$ point, as shown in Fig. 6. The hybrid density functional method has been used to confirm the existence of band inversion. Without SOC, the occupied and unoccupied low-energy bands are triply degenerate at the $R$ point. These states belong to the 3D irreducible representations $\Gamma_4^-$ and $\Gamma_5^+$ of the $O_h$ group at the $R$ point, respectively. We emphasize that the band inversion for $Cu_3PdN$ is controlled by the hopping parameter of p and d orbitals on Pd atoms, unlike the situation in a typical topological insulator such as the $Bi_2Se_3$ family compounds, which is due to SOC. The energies of $\Gamma_4^-$ and $\Gamma_5^+$ bands at the $R$ point as a function of lattice parameter are shown in Fig. 6(b), which shows that the band inversion occurs when $a < 1.11a_0$.

The low-energy effective model Hamiltonian for the two crossing bands has the same formula as expressed in Eqs. (2) and (5). In the case of $Cu_3PdN$, the Pauli matrices characterize two bands, which are mainly from
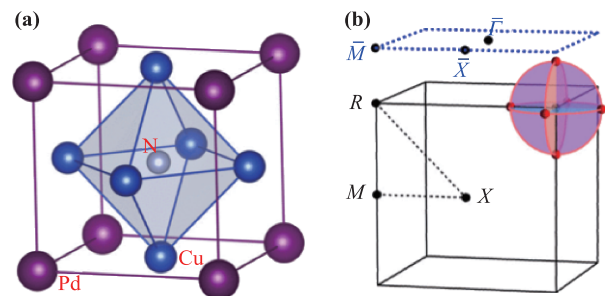


**Fig. 5** **(a)** Crystal structure of anti-perovskite $Cu_3PdN$. **(b)** Bulk and projected (001) surface BZ. The three nodal line rings (*orange color*) and three pairs of Dirac points (*red points*) without and with SOC included, respectively, are schematically shown. Reproduced from Ref. [46].
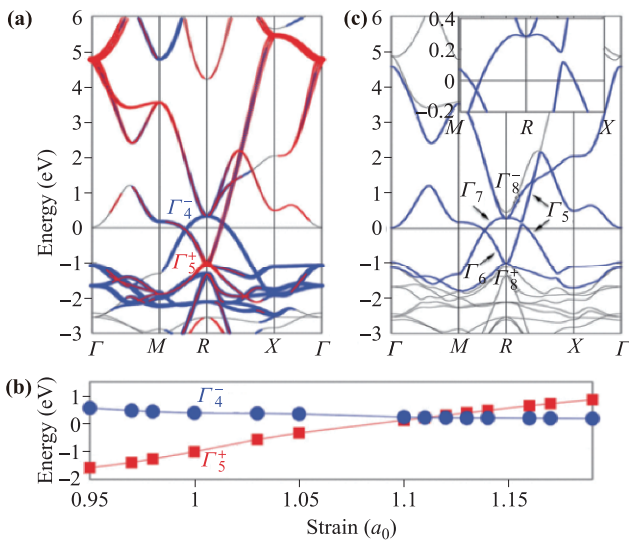
**Fig. 6** Electronic band structure **(a)** without SOC and **(c)** with SOC. The component of Pd-5$p$ (4$d$) orbitals is proportional to the width of the red (blue) curves. Band inversion between Pd-5$p$ (*red*) and Pd-4$d$ (*blue*) orbits happens at $R$ point and the nodal line exist and surround the $R$ point if SOC is ignored. A small gap is opened in the R-X direction while the Dirac point in the R-M direction is stable and protected by crystal symmetry $C_4$ rotation when SOC is take into consideration. **(b)** Evolution of $\Gamma_5^+$ and $\Gamma_4^-$ bands at $R$ point under hydrostatic pressure. Band inversion happens when $a < 1.11a_0$. Reproduced from Ref. [46].

the $p_z$ and $d_{xy}$ orbitals of Pd atoms. With the same argument as discussed for MTC, there exist closed nodal lines in Cu$_3$PdN, as the coexistence of time-reversal and spatial-inversion symmetry occurs in the case of band inversion, and the SOC is not considered. The distribution of the nodal line in momentum space is shown in Fig. 5(b), which can be understood by studying the model Hamiltonian 2 and 5.

The surface states of Cu$_3$PdN on the (001)-direction surface are calculated using the TB Hamiltonian from the maximum localized Wannier functions (MLWF) [73, 74]. The obtained band structures and surface density of states are presented in Fig. 7. The bulk state is the same as MTC, and there exists surface flat bands nestled inside the projected nodal line ring, as shown in Fig. 7(a).

In the presence of SOC, first-principles calculations indicate that a gap about 0.062 eV is opened in the $R$-$X$ direction, as shown in Fig. 6(b). An interesting finding is that the nodal point in the $R$-$M$ direction is unaffected by SOC and that the crossing bands belong to the $\Gamma_7$ and $\Gamma_6$ representation of the $C_{4v}$ double group and the coupling between them vanishes. Therefore, in the presence of SOC, the nodal lines evolve into three pairs of Dirac points, as shown in Fig. 5(b). The (001)-direction surface band structure in Fig. 7(b) clearly shows the gapped

bulk state along the $\bar{\Gamma}$-$\bar{M}$ direction and the existence of a surface Dirac cone due to topologically nontrivial Z$_2$ indexes, as observed in Na$_3$Bi [10] and Cd$_3$As$_2$ [11]. The bulk Dirac cones are hidden by other bulk states. Therefore, it is difficult to identify the detailed connection of Fermi arcs in the Fermi surface plot, as shown in Fig. 8, though some eyebrow-like Fermi arcs can be clearly seen around these projected Dirac nodes.

## 2.3 Black phosphorus under pressure

The orthorhombic bulk black phosphorus (BP) belongs to space group *Cmce* (No. 64) with a layered structure. Each layer is a 2D hexagonal Lattice, which is puckered along the armchair direction. These monolayers are stacked along the $z$ direction with van der Waals inter-
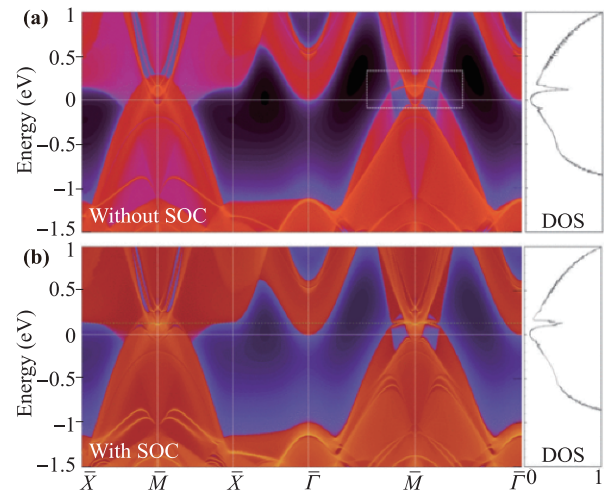


**Fig. 7** Band structures and DOS for (001) surface **(a)** without and **(b)** with SOC. Without SOC, the nearly flat surface bands are clearly shown in the white dashed box around $\bar{M}$ point. Reproduced from Ref. [46].
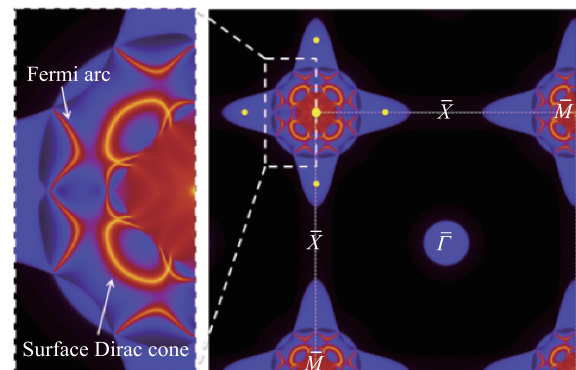


**Fig. 8** Fermi surface of (001) surface shown in Fig. 6(b) with chemical potential at 0.12 eV [green dashed line in Fig. 6(b)]. The yellow dots are projected Dirac points. The bigger one at $\bar{M}$ means there are two Dirac points superposed there. Reproduced from Ref. [46].
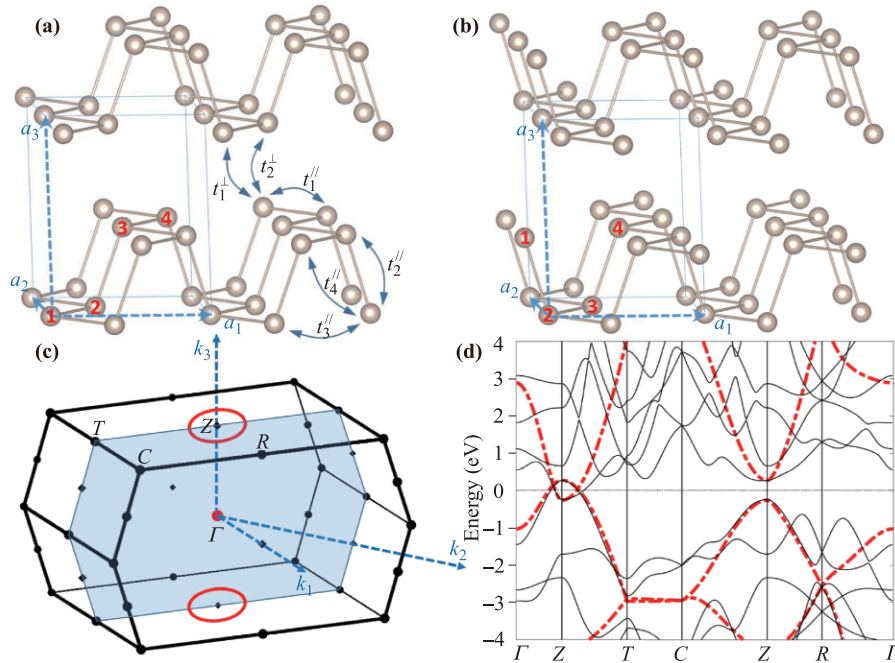
**Fig. 9** **(a)** Crystal structure of bulk BP and the hopping parameters $t_{ij}$ of the TB model. The surface in (100) direction with zigzag type and beard type surface are presented in **(a)** and **(b)** respectively. **(c)** BZ of the bulk BP. The nodal line is schematically shown with red color circle which surrounds $Z$ point and lies on the $T$-$Z$-$\Gamma$ plane. **(d)** The band structures of BP under hydrostatic pressure is shown with black color. Band structures calculated by using four-bands TB model are shown with red dashed curves. The fitted parameters read as $\epsilon = -1.1112$ eV, $t_1^{//} = -1.3298$ eV, $t_2^{//} = 4.2265$ eV, $t_3^{//} = -0.3605$ eV, $t_4^{//} = -0.1621$ eV, $t_1^{\perp} = 0.5558$ eV, $t_2^{\perp} = 0.2303$ eV. Reproduced from Ref. [58].

actions between them, as shown in Fig. 9(a). The bulk BP is a semiconductor with a gap of approximately 300 meV. Under low pressure, the energies of valence and conduction bands are inverted, and the BP becomes a semimetal [75–77].

We find that, under the pressure of $V \approx 0.88V_0$ ($V_0$ is the optimized equilibrium volume by GGA), BP has robust band inversion and well-defined semimetal features, as shown in Fig. 9(d). Near the Fermi energy, two bands with opposite parity are inverted at the $Z$ point, and a nodal line surrounds the $Z$ point in the $T$-$Z$-$\Gamma$ plane of the BZ, as shown in Fig. 9(c), which is protected by the coexistence of time-reversal and inversion symmetry. There is only one nodal line in the BP system, which is different from the MTC and anti-perovskite $Cu_3PdN$, where three nodal lines exist owing to the cubic symmetry in these systems.

There are two types of surfaces in the (100) direction: the zigzag type and the beard type, as shown in Figs. 9(a) and (b). For the zigzag surface, the calculated surface states are located outside the nodal ring, as shown in Fig. 10(a). In contrast, for the beard-type surface, a nearly flat surface state exists inside the nodal ring, as present in Fig. 10(b). In order to understand these results, we construct a simplified four-band TB model, as

expressed below:

$$H = \sum_i \epsilon_i c_i^\dagger c_i + \sum_{i \neq j} t_{ij} c_i^\dagger c_j, \tag{11}$$

where the summation $i$ runs over the lattice sites, $c_i^\dagger (c_j)$ is the creation (annihilation) operator of electrons at site $i$ ($j$), $\epsilon_i$ is the on-site energy parameter, and $t_{ij}$ is the hopping parameter between the $i$-th and $j$-th sites, as shown in Fig. 9(a). The Hamiltonian in Eq. (11) can be transformed to the momentum space as $H = \sum_k c^\dagger(k) H(k) c(k)$, where

$$H(k) = \epsilon + \begin{bmatrix} 0 & h_{12} & h_{13} & h_{14} \\ & 0 & h_{23} & h_{24} \\ & & 0 & h_{34} \\ \dagger & & & 0 \end{bmatrix}, \tag{12}$$

and

$$h_{12} = t_1^{//}(1 + e^{-ik \cdot a_2}) + t_3^{//}[e^{-ik \cdot a_1} + e^{-ik \cdot (a_1 + a_2)}],$$
$$h_{13} = t_4^{//}[1 + e^{-ik \cdot a_2} + e^{-ik \cdot a_1} + e^{-ik \cdot (a_1 + a_2)}]$$
$$\qquad + t_2^{\perp}[e^{-ik \cdot a_3} + e^{-ik \cdot (a_1 + a_3)}],$$
$$h_{14} = t_2^{//}e^{-ik \cdot (a_1 + a_2)} + t_1^{\perp}[e^{-ik \cdot (a_1 + a_3)} + e^{-ik \cdot (a_1 + a_2 + a_3)}],$$
$$h_{23} = t_2^{//} + t_1^{\perp}[e^{-ik \cdot a_3} + e^{ik \cdot (a_2 - a_3)}],$$
$$h_{24} = h_{13}, \quad h_{34} = h_{12}, \tag{13}$$

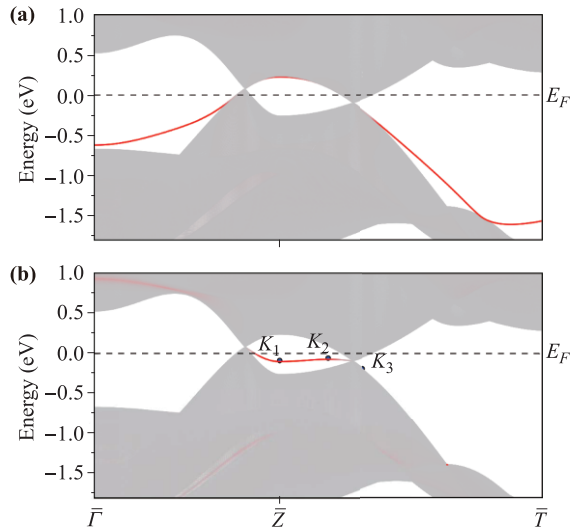*Rui Yu, et al., Front. Phys. 12(3), 127202 (2017)*

127202-7

**Fig. 10** The surface states of compressed BP on the **(a)** zigzag type and **(b)** beard type surface in the (100) direction. The surface states exist outside the nodal ring for the zigzag type surface and inside the nodal ring for the beard type surface. Reproduced from Ref. [58].

where $a_{1,2,3}$ are the lattice axis and the basis functions $(\phi_1, \phi_2, \phi_3, \phi_4)$ located on the four P-atoms in the unit cell are sketched in Fig. 9(a). Near the Fermi energy, both the valence and conduction bands are well reproduced within the energy region of $\pm 0.25$ eV, as shown in Fig. 9(d).

To investigate how the surface states are dependent on the type of surface termination, we study the one-dimensional systems parameterized by the in-plane momentum $(k_2, k_3)$ for the zigzag and beard-type surface and show that the Berry phase of such one-dimensional systems is related to the distribution of the surface states on the surface BZ. The $\pi$ Berry phase indicates that there is a surface state at the $(k_2, k_3)$ point in the surface BZ, and the vanishing of the Berry phase indicates that no surface states exist. For the zigzag-type surface, the calculated Berry phase equals $\pi$ for $(k_2, k_3)$ outside the nodal ring, while it is zero for $(k_2, k_3)$ inside the nodal ring. For the beard-type surface, the Hamiltonian matrix elements in Eq. (12) need to be expressed in the following manner:

$$h_{12} = t_2^{//} + t_1^{\perp}[e^{ik\cdot a_3} + e^{-ik\cdot(a_2-a_3)}],$$
$$h_{13} = t_4^{//}[1 + e^{-ik\cdot a_2} + e^{-ik\cdot a_1} + e^{-ik\cdot(a_1+a_2)}]$$
$$\quad + t_2^{\perp}[e^{-ik\cdot(a_2-a_3)} + e^{-ik\cdot(a_1+a_2-a_3)}],$$
$$h_{14} = t_1^{//}[e^{-ik\cdot a_1} + e^{-ik\cdot(a_1+a_2)}] + t_3^{//}(1 + e^{-ik\cdot a_2}),$$
$$h_{23} = t_1^{//}(1 + e^{-ik\cdot a_2}) + t_3^{//}[e^{-ik\cdot a_1} + e^{-ik\cdot(a_1+a_2)}],$$
$$h_{24} = t_4^{//}[1 + e^{-ik\cdot a_2} + e^{-ik\cdot a_1} + e^{-ik\cdot(a_1+a_2)}]$$
$$\quad + t_2^{\perp}[e^{-ik\cdot a_3} + e^{-ik\cdot(a_1+a_3)}],$$

$$h_{34} = t_2^{//} + t_1^{\perp}[e^{-ik\cdot a_3} + e^{ik\cdot(a_2-a_3)}], \tag{14}$$

where the basis is indicated in Fig. 9(b). The calculated Berry phase is in contrast to the zigzag case, which is in agreement with the surface states, as shown in Fig. 10(b).

## 2.4 CaP$_3$ family of materials

The crystal structure of the CaP$_3$ family of materials is closely related to the orthorhombic BP and can be derived from the latter by removing 1/4 of the P atoms, as shown in Fig. 11. Fourteen P atoms in the a-c plane form a two-dimensional puckered circle, and two Ca atoms are inserted into the circle, as shown in Figs. 11(a) and (c) [78]. These two-dimensional planes stack along the b-axis and form channels in the a-c direction with Ca atoms inserted into them, as shown in Figs. 11(b) and (d). The space group of CaP$_3$ and CaAs$_3$ is P-1, while SrP$_3$, SrAs$_3$, and BaAs$_3$ have higher symmetry characterized by space group C2/m. The band structure of the CaP$_3$ family of materials is presented in Fig. 12, where the SOC is not taken into account. The band structure obtained within the generalized gradient approximation (GGA) calculations shows that two bands with opposite parity are inverted around the Y point near the Fermi energy. The symmetry at the Y point are composed of time-reversal symmetry and space-inversion symmetry for P-1 symmetry materials and has an additional mirror symmetry for C2/m symmetry materials. The nodal line structures are found on the Γ-Y-S plane for SrP$_3$, SrAs$_3$, and BaAs$_3$, as shown
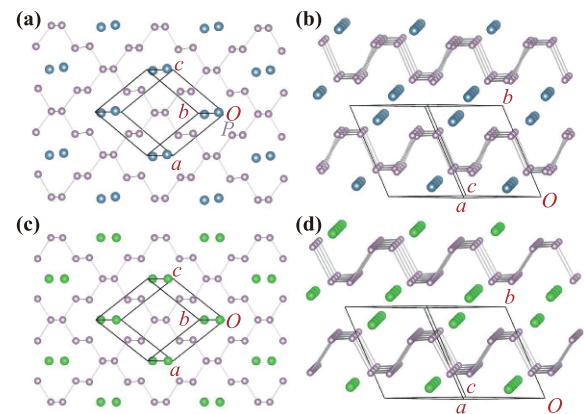


**Fig. 11** **(a)** Top view of single layer of CaP$_3$ and CaAs$_3$. The puckered P and As layers (*gray color balls*) are closely related to the orthorhombic black phosphorus and can be derived from the latter by removing 1/4 of the P atoms. **(b)** Crystal structure CaP$_3$ and CaAs$_3$. The puckered polyanionic layers stack along the b-axis. The space group for these two compounds is P-1 (No. 2). **(c)** and **(d)** for the single layer and bulk crystal structure of SrP$_3$, SrAs$_3$ and BaAs$_3$, which are characterized by space group C2/m (No. 12). Reproduced from Ref. [59].
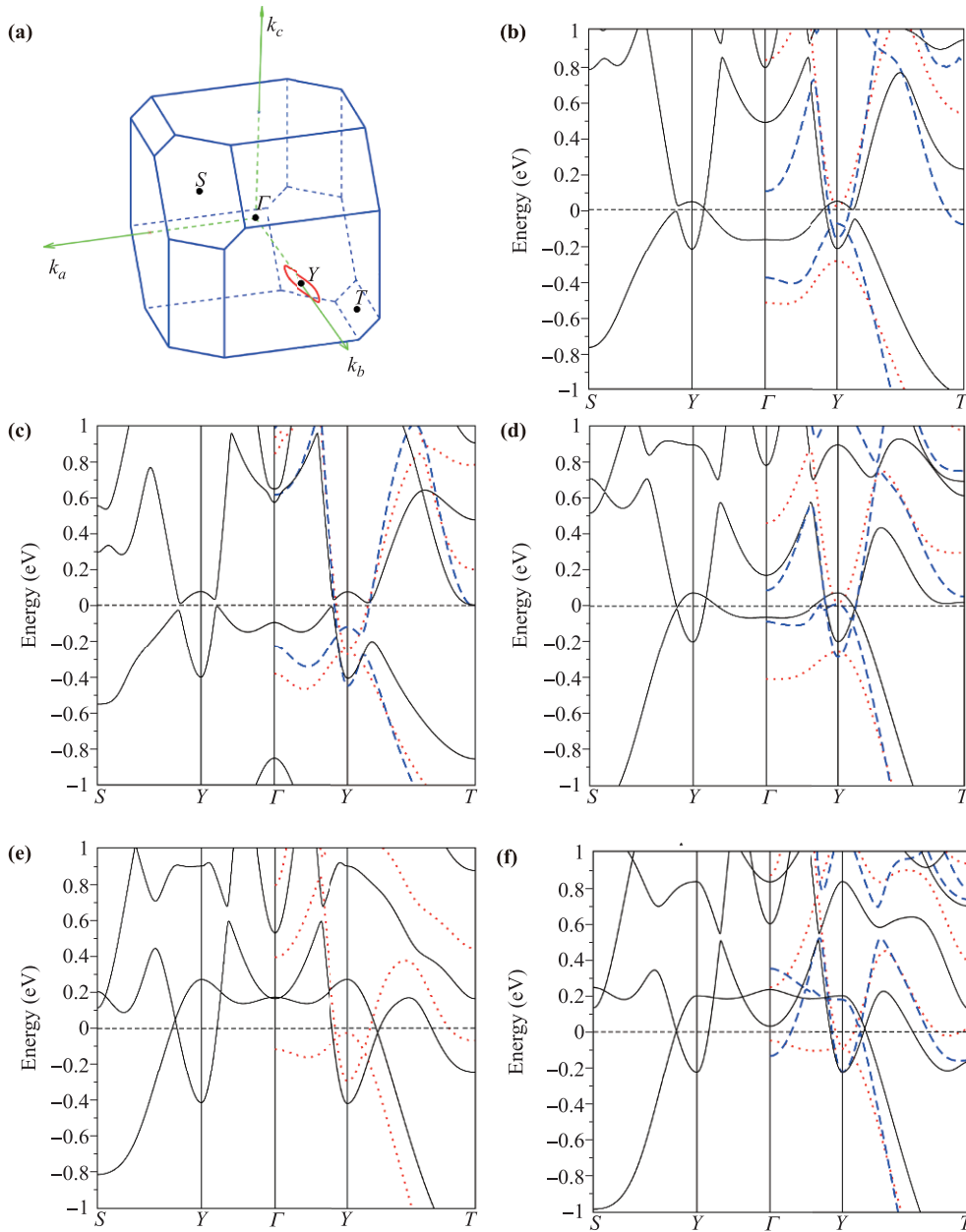
**Fig. 12** (a) The bulk BZ for CaP$_3$ family of materials. The nodal line (*red color loop*) surrounds $Y$ point and lies on the $\Gamma$-$Y$-$S$ plane for SrP$_3$, SrAs$_3$ and BaAs$_3$ compounds, while it slightly deviates from this plane for CaP$_3$ and CaAs$_3$. The band structure from GGA calculations are shown with black solid cures for **(b)** CaP$_3$, **(c)** CaAs$_3$, **(d)** SrP$_3$, **(e)** SrAs$_3$ and **(f)** BaAs$_3$. The red dotted curves are HSE06 calculation results and the blue dashed curves are HSE06 calculation results with compressed lattice structure $0.94a \times 0.94b \times 0.94c$. Reproduced from Ref. [59].

in Fig. 12(a), while for CaP$_3$ and CaAs$_3$, the nodal line is slightly deviated from this plane. We have performed the HSE06 calculations to check the band structure near the $Y$ point, which is shown by the red dotted curves in Figs. 12(b)–(f). We find that only SrAs$_3$ takes the band-inverted structure in the HSE06 calculations, while the band energies of the other four compounds are in normal order. Therefore, the nodal line structure sur-

vives in the former material but vanishes in the latter four materials. On the other hand, we also find that the compression of the lattice volume is beneficial for the emergence of band inversion. The band structures of the compressed lattice with HSE06 calculation are shown with blue dashed curves in Fig. 12. Therefore, the emergence of the nodal line in the latter four materials can be controlled by compressing the crystal lattice. The sur-
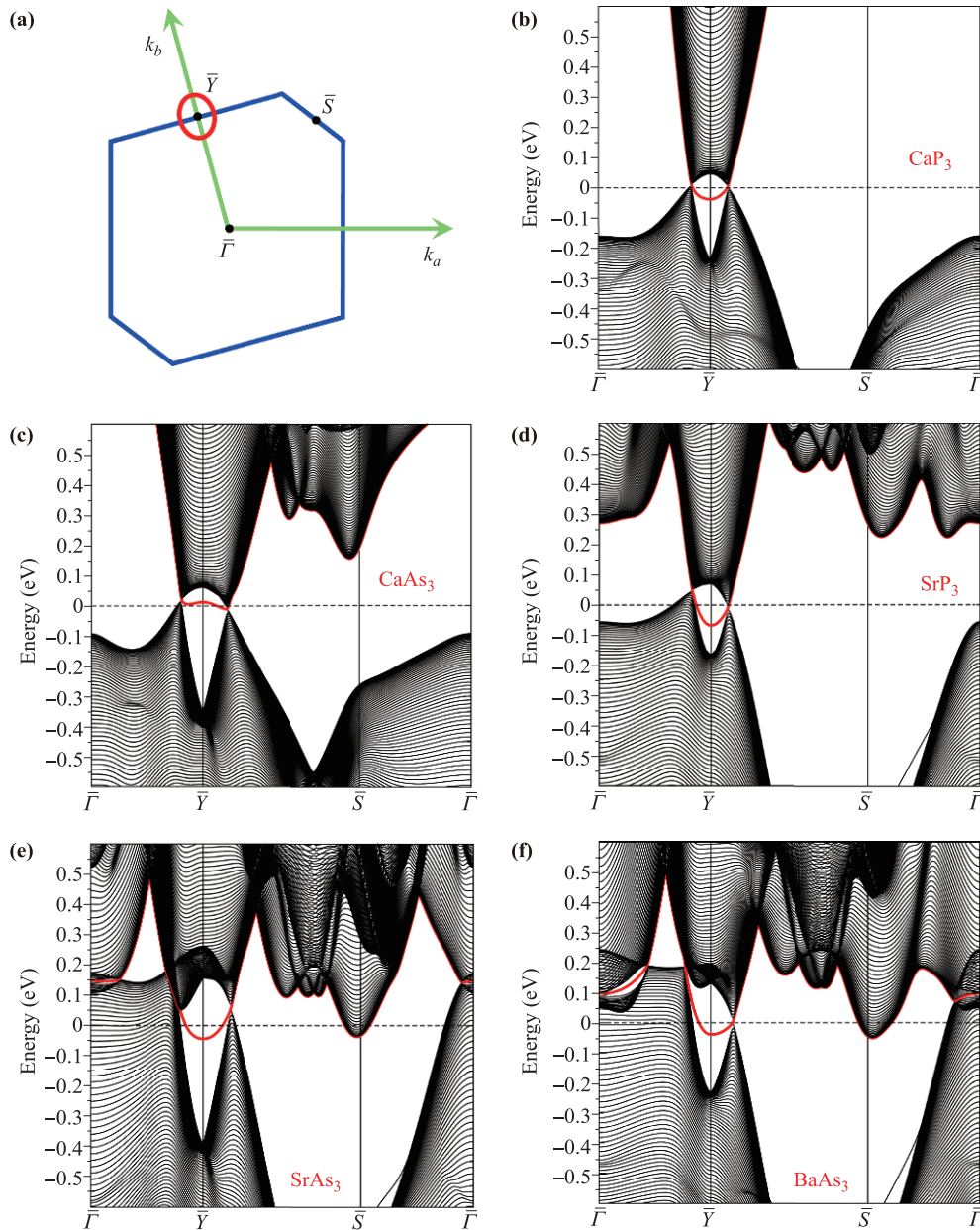
**Fig. 13** **(a)** The projected BZ along $c$-direction. The surface states (red colored curve near $Y$ point) **(b)** for CaP$_3$, **(c)** CaAs$_3$, **(d)** SrP$_3$, **(e)** SrAs$_3$ and **(f)** BaAs$_3$ are nestled between two solid Dirac cones, which are the projection of the nodal line circles. Reproduced from Ref. [59].

face states in the c-direction are shown in Figs. 13(b)–(f).

A two-band model can be constructed form the symmetry consideration. At the band-inversion point $Y$, the symmetry group is $C_i$ for *P-1* space group materials and *C2h* for *C2/m* space group materials. The $C_i$ group contains time-reversal symmetry and space-inversion symmetry. For the *C2h* group, there is an additional mirror symmetry $M : k_a \leftrightarrow k_c; k_b \rightarrow k_b$. By retaining terms up to the lowest order of $\boldsymbol{k}$, the coefficient in the Hamiltonian 2 can be expressed as

$$g_0(\boldsymbol{k}) = a_0 + a_1 k_a^2 + a_2 k_b^2 + a_3 k_c^2,$$
$$g_2(\boldsymbol{k}) = \alpha k_a + \beta k_b + \gamma k_c,$$
$$g_3(\boldsymbol{k}) = m_0 + m_1 k_a^2 + m_2 k_b^2 + m_3 k_c^2. \quad (15)$$

where the basis vectors in $\boldsymbol{k}$ space are chosen as $k_a$, $k_b$, and $k_c$, as shown in Fig. 12(a). For the *P-1* space group materials CaP$_3$ and CaAs$_3$, the parameters in Eq. (15) are independent. For the *C2/m* space group materials, the mirror symmetry can be chosen as $\hat{M} = \sigma_z$, and the mirror symmetry gives an additional constraint to the

Hamiltonian in Eq. (2):

$$\hat{M}H(k_a, k_b, k_c)\hat{M}^{-1} = H(k_c, k_b, k_a), \qquad (16)$$

which reduces the number of parameters by requiring that $\beta = 0$, $a_1 = a_3$, $m_1 = m_3$, and $\alpha = -\gamma$ in Eq. (15).

The band-crossing points appear when $g_2(\boldsymbol{k}) = 0$ and $g_3(\boldsymbol{k}) = 0$. In the band-inversion case, $g_3(\boldsymbol{k}) = m_0 + m_1 k_a^2 + m_2 k_b^2 + m_3 k_c^2 = 0$ is simply an equation for an ellipsoidal surface, which surrounds the $Y$ point in $\boldsymbol{k}$ space. $g_2(\boldsymbol{k}) = \alpha k_a + \beta k_b + \gamma k_c = 0$ determines a plane passing the $Y$ point having its normal direction along $(\alpha, \beta, \gamma)$. The crossing line between the plane and the ellipsoidal surface is the nodal line in the BZ. For the $C2/m$ space group, where $\beta = 0$ and $\alpha = -\gamma$, the nodal line lies on the plane that passes through $k_b$ and the angular bisector of $k_a$ and $k_c$. The higher-order terms, such as the fourth-order terms in $g_{0,3}(\boldsymbol{k})$ and the third-order terms in $g_2(\boldsymbol{k})$, will deform the ellipsoidal surface and bend the plane; nevertheless, the crossing nodal line does not disappear and instead changes to a three-dimensional closed loop, as shown in Fig. 12(a).

If the SOC is taken into consideration, gaps will be opened along the nodal line, and these materials become small-gap topological insulators. The SOC gap along $S$-$Y$ and $Y$-$\Gamma$ directions are listed in Table 1.

## 3  Discussion and future prospects

In this review, we proposed four materials that have a nodal line structure near the Fermi energy by following the design principle that the system needs to have a coexistence of time-reversal symmetry and inversion symmetry in the case with band inversion and negligible SOC. Therefore, one needs to search for a material composed of light elements with negligible SOC. From this perspective, photonic crystals and phononic crystals are the ideal platforms to realize the nodal line structure because there is no spin degree of freedom in these two types of systems. For the component with heavy elements, the SOC cannot be ignored, and the SOC usually destroys the nodal line structure. Nevertheless, the SOC might

**Table 1** The gap values near the nodal line after considering the SOC.

|        | $S - Y$    | $Y - \Gamma$ |
|--------|------------|--------------|
| $CaP_3$  | 31.69 meV  | 3.73 meV     |
| $CaAs_3$ | 54.47 meV  | 39.92 meV    |
| $SrP_3$  | 6.11 meV   | 1.76 meV     |
| $SrAs_3$ | 47.14 meV  | 6.28 meV     |
| $BaAs_3$ | 38.97 meV  | 6.22 meV     |

drive the nodal line state into new topological states. For example, the SOC drives the nodal line structure in $Cu_3PdN$ into Dirac points and converts the nodal line in TaAs into Weyl points. Therefore, the nodal line states can be thought of as an intermediate phase, starting from which one can obtain other topological phases [79]. On the other hand, the nodal line structure can stably exist in the systems with strong SOC, which have an additional symmetry besides the time-reversal and inversion symmetry. For example, double-nodal lines are proposed in the system with additional twofold screw rotation [4].

Though many nodal line materials have been proposed thus far, experimental reports on nodal-line materials are rare. An interesting and valuable direction for future work is to find more materials that can be confirmed by experiments. More physical characteristics related to the nodal line structure need to be studied to facilitate its experimental confirmation. It is also interesting to study the coexistence of the nodal line semimetals with other effects, such as the electronic correlation effect, superconductivity, and magnetism.

## References

1. G. E. Volovik, The Universe in a Helium Droplet, Oxford, 2009

2. Z. Fang, N. Nagaosa, K. S. Takahashi, A. Asamitsu, R. Mathieu, T. Ogasawara, H. Yamada, M. Kawasaki, Y. Tokura, and K. Terakura, The anomalous Hall effect and magnetic monopoles in momentum space, *Science* 302(5642), 92 (2003)

3. H. Weng, R. Yu, X. Hu, X. Dai, and Z. Fang, Quantum anomalous Hall effect and related topological electronic states, *Adv. Phys.* 64(3), 227 (2015)

4. C. Fang, Y. Chen, H. Y. Kee, and L. Fu, Topological nodal line semimetals with and without spin-orbital coupling, *Phys. Rev. B* 92(8), 081201 (2015)

5. Y. X. Zhao, A. P. Schnyder, and Z. D. Wang, Unified theory of PT and CP invariant topological metals and nodal superconductors, *Phys. Rev. Lett.* 116(15), 156402 (2016)

6. H. B. Nielsen and M. Ninomiya, The Adler–Bell–Jackiw anomaly and Weyl fermions in a crystal, *Phys. Lett. B* 130(6), 389 (1983)

*Rui Yu, et al., Front. Phys. 12(3), 127202 (2017)*

127202-11

7. X. Wan, A. M. Turner, A. Vishwanath, and S. Y. Savrasov, Topological semimetal and Fermi-arc surface states in the electronic structure of pyrochlore iridates, *Phys. Rev. B* 83(20), 205101 (2011)

8. G. Xu, H. Weng, Z. Wang, X. Dai, and Z. Fang, Chern semimetal and the quantized anomalous Hall effect in $HgCr_2Se_4$, *Phys. Rev. Lett.* 107(18), 186806 (2011)

9. L. Balents, Weyl electrons kiss, *Physics* 4, 36 (2011)

10. Z. Wang, Y. Sun, X. Q. Chen, C. Franchini, G. Xu, H. Weng, X. Dai, and Z. Fang, Dirac semimetal and topological phase transitions in $A_3Bi$ (A = Na, K, Rb), *Phys. Rev. B* 85(19), 195320 (2012)

11. Z. Wang, H. Weng, Q. Wu, X. Dai, and Z. Fang, Three dimensional Dirac semimetal and quantum transport in $Cd_3As_2$, *Phys. Rev. B* 88(12), 125427 (2013)

12. A. A. Burkov, M. D. Hook, and L. Balents, Topological nodal semimetals, *Phys. Rev. B* 84(23), 235126 (2011)

13. H. Weng, Y. Liang, Q. Xu, R. Yu, Z. Fang, X. Dai, and Y. Kawazoe, Topological node-line semimetal in three dimensional graphene networks, arxiv: 1411.2175

14. B. J. Yang and N. Nagaosa, Classification of stable three-dimensional Dirac semimetals with nontrivial topology, *Nat. Commun.* 5, 4898 (2014)

15. A. Pariari, P. Dutta, and P. Mandal, Probing the Fermi surface of three-dimensional Dirac semimetal $Cd_3As_2$ through the de Haas–van Alphen technique, *Phys. Rev. B* 91(15), 155139 (2015)

16. L. P. He, X. C. Hong, J. K. Dong, J. Pan, Z. Zhang, J. Zhang, and S. Y. Li, Quantum transport evidence for the three-dimensional Dirac semimetal phase in $Cd_3As_2$, *Phys. Rev. Lett.* 113(24), 246402 (2014)

17. M. Neupane, S. Y. Xu, R. Sankar, N. Alidoust, G. Bian, C. Liu, I. Belopolski, T. R. Chang, H. T. Jeng, H. Lin, A. Bansil, F. Chou, and M. Z. Hasan, Observation of a three-dimensional topological Dirac semimetal phase in high-mobility $Cd_3As_2$, *Nat. Commun.* 5, 3786 (2014)

18. Z. K. Liu, B. Zhou, Y. Zhang, Z. J. Wang, H. M. Weng, D. Prabhakaran, S. K. Mo, Z. X. Shen, Z. Fang, X. Dai, Z. Hussain, and Y. L. Chen, Discovery of a three dimensional topological Dirac semimetal, $Na_3Bi$, *Science* 343(6173), 864 (2014)

19. Z. K. Liu, J. Jiang, B. Zhou, Z. J. Wang, Y. Zhang, H. M. Weng, D. Prabhakaran, S. K. Mo, H. Peng, P. Dudin, T. Kim, M. Hoesch, Z. Fang, X. Dai, Z. X. Shen, D. L. Feng, Z. Hussain, and Y. L. Chen, A stable three dimensional topological Dirac semimetal $Cd_3As_2$, *Nat. Mater.* 13(7), 677 (2014)

20. Q. D. Gibson, L. M. Schoop, L. Muechler, L. S. Xie, N. P. Ong, M. Hirschberger, R. Car, and R. J. Cava, Three-dimensional Dirac semimetals: Design principles and predictions of new materials, *Phys. Rev. B* 91(20), 205128 (2015)

21. H. Weng, C. Fang, Z. Fang, B. A. Bernevig, and X. Dai, Weyl semimetal phase in noncentrosymmetric transition-metal monophosphides, *Phys. Rev. X* 5(1), 011029 (2015)

22. S. M. Huang, S. Y. Xu, I. Belopolski, C. C. Lee, G. Chang, B. Wang, N. Alidoust, G. Bian, M. Neupane, C. Zhang, S. Jia, A. Bansil, H. Lin, and M. Z. Hasan, A Weyl fermion semimetal with surface Fermi arcs in the transition metal monopnictide TaAs class, *Nat. Commun.* 6, 7373 (2015)

23. A. A. Soluyanov, D. Gresch, Z. Wang, Q. S. Wu, M. Troyer, X. Dai, and B. A. Bernevig, Type-II Weyl semimetals, *Nature* 527(7579), 495 (2015)

24. B. Q. Lv, H. M. Weng, B. B. Fu, X. P. Wang, H. Miao, J. Ma, P. Richard, X. C. Huang, L. X. Zhao, G. F. Chen, Z. Fang, X. Dai, T. Qian, and H. Ding, Experimental discovery of Weyl semimetal TaAs, *Phys. Rev. X* 5(3), 031013 (2015)

25. X. Huang, L. Zhao, Y. Long, P. Wang, D. Chen, Z. Yang, H. Liang, M. Xue, H. Weng, Z. Fang, X. Dai, and G. Chen, Observation of the chiral-anomaly-induced negative magnetoresistance in 3d Weyl semimetal TaAs, *Phys. Rev. X* 5(3), 031023 (2015)

26. B. Q. Lv, N. Xu, H. M. Weng, J. Z. Ma, P. Richard, X. C. Huang, L. X. Zhao, G. F. Chen, C. E. Matt, F. Bisti, V. N. Strocov, J. Mesot, Z. Fang, X. Dai, T. Qian, M. Shi, and H. Ding, Observation of Weyl nodes in TaAs, *Nat. Phys.* 11(9), 724 (2015)

27. S. Y. Xu, I. Belopolski, N. Alidoust, M. Neupane, G. Bian, C. Zhang, R. Sankar, G. Chang, Z. Yuan, C. C. Lee, S. M. Huang, H. Zheng, J. Ma, D. S. Sanchez, B. Wang, A. Bansil, F. Chou, P. P. Shibayev, H. Lin, S. Jia, and M. Z. Hasan, Discovery of a Weyl fermion semimetal and topological Fermi arcs, *Science* 349(6248), 613 (2015)

28. N. Xu, H. M. Weng, B. Q. Lv, C. E. Matt, J. Park, F. Bisti, V. N. Strocov, D. Gawryluk, E. Pomjakushina, K. Conder, N. C. Plumb, M. Radovic, G. Autès, O. V. Yazyev, Z. Fang, X. Dai, T. Qian, J. Mesot, H. Ding, and M. Shi, Observation of Weyl nodes and Fermi arcs in tantalum phosphide, *Nat. Commun.* 7, 11006 (2016)

29. B. Q. Lv, S. Muff, T. Qian, Z. D. Song, S. M. Nie, N. Xu, P. Richard, C. E. Matt, N. C. Plumb, L. X. Zhao, G. F. Chen, Z. Fang, X. Dai, J. H. Dil, J. Mesot, M. Shi, H. M. Weng, and H. Ding, Observation of Fermi-arc spin texture in TaAs, *Phys. Rev. Lett.* 115(21), 217601 (2015)

30. G. Chang, S.Y. Xu, D. S. Sanchez, S.M. Huang, C.C. Lee, T.R. Chang, H. Zheng, G. Bian, I. Belopolski, N. Alidoust, H.T. Jeng, A. Bansil, H. Lin, and M. Z. Hasan, A strongly robust Weyl fermion semimetal state in $Ta_3S_2$, arXiv: 1512.08781

31. J. Ruan, S. K. Jian, D. Zhang, H. Yao, H. Zhang, S. C. Zhang, and D. Xing, Ideal Weyl Semimetals in the Chalcopyrites $CuTlSe_2$, $AgTlTe_2$, $AuTlTe_2$, and $ZnPbAs_2$, *Phys. Rev. Lett.* 116(22), 226801 (2016)

32. J. Ruan, S. K. Jian, H. Yao, H. Zhang, S. C. Zhang, and D. Xing, Symmetry-protected ideal Weyl semimetal in HgTe-class materials, *Nat. Commun.* 7, 11136 (2016)

127202-12

*Rui Yu, et al., Front. Phys. 12(3), 127202 (2017)*

**Frontiers of Physics**

33. M. Hirschberger, S. Kushwaha, Z. Wang, Q. Gibson, S. Liang, C. A. Belvin, B. A. Bernevig, R. J. Cava, and N. P. Ong, The chiral anomaly and thermopower of Weyl fermions in the half-Heusler GdPtBi, *Nat. Mater.* (2016), arXiv: 1602.07219

34. Z. Wang, M. G. Vergniory, S. Kushwaha, M. Hirschberger, E. V. Chulkov, A. Ernst, N. P. Ong, R. J. Cava, and B. A. Bernevig, Time-reversal breaking Weyl fermions in magnetic Heuslers, arXiv: 1603.00479

35. G. Autès, D. Gresch, M. Troyer, A. A. Soluyanov, and O. V. Yazyev, Robust type-II Weyl semimetal phase in transition metal diphosphides $XP_2$ (X = Mo, W), *Phys. Rev. Lett.* 117(6), 066402 (2016)

36. C. K. Chiu and A. P. Schnyder, Classification of reflection-symmetry-protected topological semimetals and nodal superconductors, *Phys. Rev. B* 90(20), 205136 (2014)

37. T. T. Heikkilä, N. B. Kopnin, and G. E. Volovik, Flat bands in topological media, *JETP Lett.* 94(3), 233 (2011)

38. T. T. Heikkilä and G. E. Volovik, Dimensional crossover in topological matter: Evolution of the multiple Dirac point in the layered system to the flat band on the surface, *JETP Lett.* 93(2), 59 (2011)

39. T. T. Heikkila and G. E. Volovik, Flat bands as a route to high-temperature superconductivity in graphite, arXiv: 1504.05824

40. H. Weng, Y. Liang, Q. Xu, R. Yu, Z. Fang, X. Dai, and Y. Kawazoe, Topological node-line semimetal in three dimensional graphene networks, *Phys. Rev. B* 92(4), 045108 (2015)

41. K. Mullen, B. Uchoa, and D. T. Glatzhofer, Line of Dirac nodes in hyperhoney comb lattices, *Phys. Rev. Lett.* 115(2), 026403 (2015)

42. M. Ezawa, Loop-nodal and point-nodal semimetals in three-dimensional honeycomb lattices, *Phys. Rev. Lett.* 116(12), 127202 (2016)

43. L. S. Xie, L. M. Schoop, E. M. Seibel, Q. D. Gibson, W. Xie, and R. J. Cava, A new form of $Ca_3P_2$ with a ring of Dirac nodes, *APL Mater.* 3(8), 083602 (2015)

44. Y. H. Chan, C. K. Chiu, M. Y. Chou, and A. P. Schnyder, $Ca_3P_2$ and other topological semimetals with line nodes and drumhead surface states, *Phys. Rev. B* 93(20), 205132 (2016)

45. M. Zeng, C. Fang, G. Chang, Y.-A. Chen, T. Hsieh, A. Bansil, H. Lin, and L. Fu, Topological semimetals and topological insulators in rare earth monopnictides, arXiv: 1504.03492

46. R. Yu, H. Weng, Z. Fang, X. Dai, and X. Hu, Topological node-line semimetal and Dirac semimetal state in antiperovskite $Cu_3PdN$, *Phys. Rev. Lett.* 115(3), 036807 (2015)

47. Y. Kim, B. J. Wieder, C. L. Kane, and A. M. Rappe, Dirac line nodes in inversion-symmetric crystals, *Phys. Rev. Lett.* 115(3), 036806 (2015)

48. Y. Chen, Y. Xie, S. A. Yang, H. Pan, F. Zhang, M. L. Cohen, and S. Zhang, Nanostructured carbon allotropes with Weyl-like loops and points, *Nano Lett.* 15(10), 6974 (2015)

49. G. Bian, T. R. Chang, H. Zheng, S. Velury, S. Y. Xu, T. Neupert, C. K. Chiu, S. M. Huang, D. S. Sanchez, I. Belopolski, N. Alidoust, P. J. Chen, G. Chang, A. Bansil, H. T. Jeng, H. Lin, and M. Z. Hasan, Drumhead surface states and topological nodal-line fermions in $TlTaSe_2$, *Phys. Rev. B* 93(12), 121113 (2016)

50. G. Bian, T.-R. Chang, R. Sankar, S.-Y. Xu, H. Zheng, T. Neupert, C.-K. Chiu, S.-M. Huang, G. Chang, I. Belopolski, D. S. Sanchez, M. Neupane, N. Alidoust, C. Liu, B. Wang, C.-C. Lee, H.-T. Jeng, A. Bansil, F. Chou, H. Lin, and M. Zahid Hasan, Topological nodal-line fermions in the non-centrosymmetric superconductor compound $PbTaSe_2$, arXiv: 1505.03069

51. L. M. Schoop, M. N. Ali, C. Straßer, A. Topp, A. Varykhalov, D. Marchenko, V. Duppel, S. S. P. Parkin, B. V. Lotsch, and C. R. Ast, Dirac cone protected by non-symmorphic symmetry and three dimensional Dirac line node in ZrSiS, *Nat. Commun.* 7, 11696 (2016)

52. J. M. Carter, V. V. Shankar, M. A. Zeb, and H. Y. Kee, Semimetal and topological insulator in perovskite iridates, *Phys. Rev. B* 85(11), 115105 (2012)

53. H. S. Kim, Y. Chen, and H. Y. Kee, Surface states of perovskite iridates $AIrO_3$: Signatures of a topological crystalline metal with nontrivial $Z_2$ index, *Phys. Rev. B* 91(23), 235103 (2015)

54. J. Liu, D. Kriegner, L. Horak, D. Puggioni, C. Rayan Serrao, R. Chen, D. Yi, C. Frontera, V. Holy, A. Vishwanath, J. M. Rondinelli, X. Marti, and R. Ramesh, Strain-induced nonsymmorphic symmetry breaking and removal of Dirac semimetallic nodal line in an orthoperovskite iridate, *Phys. Rev. B* 93(8), 085118 (2016)

55. Y. Chen, Y. M. Lu, and H. Y. Kee, Topological crystalline metal in orthorhombic perovskite iridates, *Nat. Commun.* 6, 6593 (2015)

56. A. Yamakage, Y. Yamakawa, Y. Tanaka, and Y. Okamoto, Line-node Dirac semimetal and topological insulating phase in noncentrosymmetric pnictides CaAgX (X = P, As), *JPSJ* 85(1), 013708 (2016)

57. Q. F. Liang, J. Zhou, R. Yu, Z. Wang, and H. Weng, Node-surface and node-line fermions from nonsymmorphic lattice symmetries, *Phys. Rev. B* 93(8), 085427 (2016)

58. J. Zhao, R. Yu, H. Weng, and Z. Fang, Topological node-line semimetal in compressed black phosphorus, arXiv: 1511.05704

59. Q. Xu, R. Yu, Z. Fang, X. Dai, and H. Weng, Topological nodal line semimetals in $CaP_3$ family of materials, arXiv: 1608.03172

60. M. Hirayama, R. Okugawa, T. Miyake, and S. Murakami, Topological Dirac nodal lines in fcc calcium, strontium, and ytterbium, arXiv: 1602.06501

*Rui Yu, et al., Front. Phys. 12(3), 127202 (2017)*

127202-13

Frontiers of Physics

61. J. T. Wang, H. Weng, S. Nie, Z. Fang, Y. Kawazoe, and C. Chen, Body-centered orthorhombic $C_{16}$: A novel topological node-line semimetal, *Phys. Rev. Lett.* 116(19), 195501 (2016)

62. R. Li, H. Ma, X. Cheng, S. Wang, D. Li, Z. Zhang, Y. Li, and X. Q. Chen, Dirac node lines in pure alkali earth metals, *Phys. Rev. Lett.* 117(9), 096401 (2016)

63. J. L. Lu, W. Luo, X. Y. Li, S. Q. Yang, J. X. Cao, X. G. Gong, and H. J. Xiang, Two-dimensional node-line semimetals in a Honeycomb-Kagome lattice, arXiv: 1603.04596

64. Y. Jin, R. Wang, J. Zhao, C. Zheng, L.Y. Gan, J. Liu, H. Xu, and S. Y. Tong, A family group of two dimensional node-line semimetals, arXiv: 1608.05791

65. G. E. Volovik, The Topology of the Quantum Vacuum, Analogue Gravity Phenomenology, Lecture Notes in Physics, Vol. 870, p. 343 (2013)

66. N. B. Kopnin, T. T. Heikkila, and G. E. Volovik, High-temperature surface superconductivity in topological flat-band systems, *Phys. Rev. B* 83(22), 220503 (2011)

67. G. E. Volovik, From standard model of particle physics to room-temperature superconductivity, *Phys. Scr.* 2015(T164), 014014 (2015)

68. T. T. Heikkila and G. E. Volovik, Flat bands as a route to high-temperature superconductivity in graphite, arXiv: 1504.05824

69. J. W. Rhim and Y. B. Kim, Landau level quantization and almost flat modes in three-dimensional semimetals with nodal ring spectra, *Phys. Rev. B* 92(4), 045126 (2015)

70. Z. Yan, P. W. Huang, and Z. Wang, Collective modes in nodal line semimetals, *Phys. Rev. B* 93(8), 085138 (2016)

71. A. L. Mackay, Periodic minimal surfaces, *Nature* 314(6012), 604 (1985)

72. R. S. K. Mong and V. Shivamoggi, Edge states and the bulk-boundary correspondence in Dirac hamiltonians, *Phys. Rev. B* 83(12), 125109 (2011)

73. A. A. Mostofi, J. R. Yates, Y. S. Lee, I. Souza, D. Vanderbilt, and N. Marzari, wannier90: A tool for obtaining maximally-localised Wannier functions, *Comput. Phys. Commun.* 178(9), 685 (2008)

74. N. Marzari, A. A. Mostofi, J. R. Yates, I. Souza, and D. Vanderbilt, Maximally localized Wannier functions: Theory and applications, *Rev. Mod. Phys.* 84(4), 1419 (2012)

75. R. Fei, V. Tran, and L. Yang, Topologically protected Dirac cones in compressed bulk black phosphorus, *Phys. Rev. B* 91(19), 195319 (2015)

76. Z. J. Xiang, G. J. Ye, C. Shang, B. Lei, N. Z. Wang, K. S. Yang, D. Y. Liu, F. B. Meng, X. G. Luo, L. J. Zou, Z. Sun, Y. Zhang, and X. H. Chen, Pressure-induced electronic transition in black phosphorus, *Phys. Rev. Lett.* 115(18), 186403 (2015)

77. K. Akiba, A. Miyake, Y. Akahama, K. Matsubayashi, Y. Uwatoko, H. Arai, Y. Fuseya, and M. Tokunaga, Anomalous quantum transport properties in semimetallic black phosphorus, *J. Phys. Soc. Jpn.* 84(7), 073708 (2015)

78. W. Dahlmann and H. G. v. Schnering, $CaP_3$, ein neues Calciumphosphid, *Naturwissenschaften* 60(11), 518 (1973)

79. Z. Yan and Z. Wang, Tunable Weyl points in periodically driven nodal line semimetals, *Phys. Rev. Lett.* 117(8), 087402 (2016)

**Frontiers of Physics**